11. Scanning Electron Microscopy with Polarization Analysis: Studies of Magnetic Microstructure

J. Unguris, M.R. Scheinfein, R.J. Celotta and D.T. Pierce

National Institute of Standards and Technology, Gaithersburg, MD 20899, USA

When a beam of electrons with energies greater than several hundred eV is incident upon a ferromagnetic metal, spin polarized secondary electrons are emitted. The polarization of these secondary electrons is related to the polarization of the electrons in the ferromagnet. In the case of transition metal ferromagnets, the polarization of the secondary electrons is directly proportional to the magnetization. Spin polarization analysis of the secondary electrons, therefore, provides a direct measurement of the magnetization in the region probed by the incident electron beam. Scanning electron microscopy with polarization analysis (SEMPA), illustrated schematically in Fig. 11.1, combines the finely focused beam of the scanning electron microscope with secondary electron spin polarization analysis to obtain a technique that provides high resolution images of the surface magnetic microstructure of ferromagnetic materials. The purpose of this chapter is to review the SEMPA technique and to present several examples of magnetic microstructures that were studied using SEMPA.

SEMPA is the product of extensive research, which began in the late 1960s, studying the emission and scattering of spin polarized electrons from solid sur-

Incident Electrons From Scanning Electron Microscope

Spin-Polarization Analyzer

Spin-Polarized Secondary Electrons
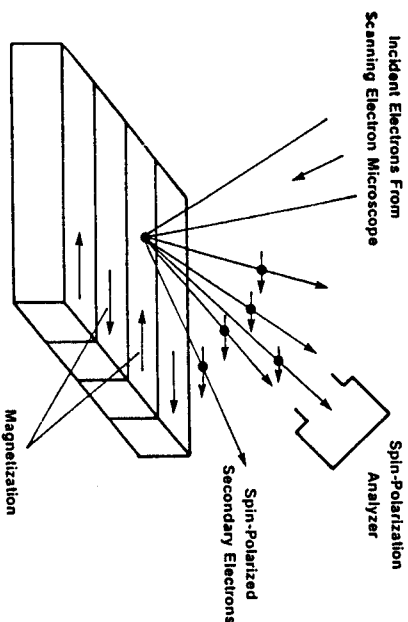
Magnetization

Fig. 11.1. Schematic diagram illustrating the SEMPA technique. A ferromagnetic specimen is scanned by the focused electron beam of a scanning electron microscope. A spin polarimeter is used to measure the polarization of the emitted secondary electrons. The spin polarization of the secondary electrons is directly proportional to the magnetization, so that a rastered image of the magnetic microstructure is produced

faces. Several reviews of this work are available [11.1-4]. The possibility of using the spin polarization of secondary electrons to image magnetic microstructure was initially discussed in the early 1980s [11.5-7]. By the mid 1980s the first SEMPA measurements had been made [11.8,9]. Most of this early SEMPA work has already been reviewed [11.10-12].

Motivation for the development of SEMPA has come primarily from the need to look at very small, sub-micron, magnetic structures, such as domain configurations and domain walls. Interest in these magnetic microstructures ranges from fundamental research studying the physics of low dimensional magnetic systems to application oriented problems in magnetic recording and fine particle permanent magnets. Conventional magnetic imaging techniques such as domain wall decoration using the Bitter method [11.13] or polarized light magneto-optic Kerr microscopy [11.14,15] are optical techniques with a resolution limit of about 0.5 micron. Higher resolution is achieved with electron microscope based techniques such as Lorentz microscopy in reflection [11.16] or transmission [11.17,18], and electron holography [11.19]. Transmission Lorentz microscopy and electron holography offer the highest resolution, on the order of 10 nm, but both techniques require thin (less than 100 nm thick) unsupported specimens. The most recently developed technique, magnetic force microscopy [11.20], is magnetic force microscopy [11.20]. The ultimate resolution of the magnetic force microscope is uncertain because of interactions between the tip and sample. All of the magnetic observation techniques, except for magneto-optic Kerr microscopy, derive magnetic contrast from their sensitivity to magnetic fields, either inside or outside of the sample, rather than magnetization. In contrast, SEMPA is a high resolution, domain imaging technique in which the signal contrast is directly related to the direction and magnitude of the magnetization. In addition, SEMPA can be applied to both thick specimens or thin films grown on thick substrates.

11.1 Spin Polarization of Secondary Electrons

The secondary electron spin polarization from ferromagnetic materials has been extensively studied for the past ten years. A recent review of much of this work is available [11.21]. Measurements of the intensity, $N(E)$, and polarization, $P(E)$, energy distributions of secondary electrons generated from transition metal ferromagnets have general features that are illustrated schematically in Fig. 11.2. The polarization component along some direction is defined as

$$P = \frac{N_\uparrow - N_\downarrow}{N_\uparrow + N_\downarrow},$$

(11.1)

where $N_\uparrow(N_\downarrow)$ are the number of electrons with spins parallel (antiparallel) to the specified direction. The polarization distributions have the following common features: First, the direction of the polarization is exactly opposite to that of the magnetization. The polarization direction of the electrons with their negative magnetic moments is not changed by the emission process. Second, the

N (E)

$$P = \frac{N_\uparrow - N_\downarrow}{N_\uparrow + N_\downarrow}$$
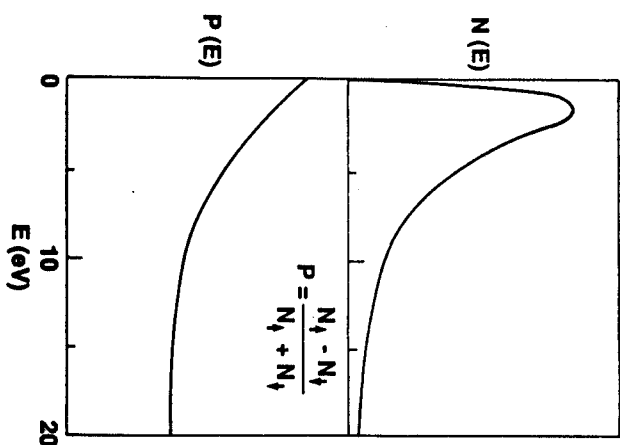
P (E)

0   10   20

E (eV)

Fig. 11.2. Schematic drawing showing the energy dependence of the intensity, $N(E)$, and polarization, $P(E)$, of secondary electrons emitted from a simple transition metal ferromagnet

polarization is relatively constant for energies greater than 10 eV except for occasional characteristic loss features. And finally, the polarization increases as the secondary electron energy approaches zero.

Some quantitative understanding of the polarization distribution can be gained by assuming that only the valence electrons contribute to the secondary electron polarization. This would apply, for example, to the transition metals, Fe, Co, or Ni, in which the orbital magnetic moment is quenched. The magnetization, M, is then related to the next spin density, $n_\uparrow - n_\downarrow$, by

$$M = -\mu_B(n_\uparrow - n_\downarrow), \qquad (11.2)$$

where μ_B is the electron magnetic moment or Bohr magneton. If the secondary electrons were simply valence electrons that were emitted without changing their polarization the secondary polarization should be equal to

$$P_v = n_b/n_v, \qquad (11.3)$$

where n_b is the magnetic moment per atom, and n_v the number of valence electrons per atom. This simple model predicts polarizations of 28%, 19%, and 5% for Fe, Co, and Ni, respectively. These values agree well with polarizations measured for energies above 10 eV for Fe [11.22], Co [11.22], and Ni [11.23].

The enhancement of the secondary polarization at low secondary electron energies is due to a spin dependent filtering of the slow secondary electrons. As the kinetic energy of the secondary electron becomes smaller, the probability that

it will lose energy and drop down into an unoccupied state below the vacuum level increases. The spin polarization enhancement is the result of there being more empty minority states than majority states available to de-excite into. This spin filter model gives good quantitative agreement with the observed low energy polarization enhancement [11.24,25]. A slightly different approach to describe the enhancement of secondary electron polarization at low energies has also been proposed which emphasizes the role of Stoner excitations in the magnetization mechanism [11.26-28]. In general, though, the relationship between the magnetization of a transition metal and the polarization of the secondary electrons emitted from it is relatively well understood. Note, however, that for ferromagnets with different electronic structures such as the rare earths, the relationship between polarization and magnetization is probably more complicated.

Another important feature of the secondary electrons is their surface sensitivity. The incident electron beam deposits its energy and, therefore, creates secondary electrons deep within the material, but only those that are close enough to the surface can escape before losing their energy [11.29]. The exact escape depth of the secondary electrons is still unresolved. If the inelastic mean free path [11.30] is used to determine the escape depth, then the secondaries are emitted from the top 2 to 3 nm of the sample. If the transport decay length [11.21] associated with a continuous slowing down of the electrons is used then escape depths of about 1 nm are predicted. In addition, there may be the further complication that the magnetic probing depth [11.31] may be different from the escape depth. More experimental work measuring the probing or escape depth of secondaries from ferromagnetic materials would be extremely valuable.

In summary, the features of polarized secondary electron emission that make SEMPA a useful tool are: First, the polarization is directly proportional to the magnetization of transition metal ferromagnets. Second, there are a lot of secondary electrons and they have relatively large polarizations so that there is a large signal to measure. And finally, the secondaries come from the outermost few atomic layers of the material.

11.2 Experimental

A schematic drawing of the SEMPA apparatus at the National Institute of Standards and Technology (NIST) is shown in Fig. 11.3. Versions of SEMPA instruments developed in different laboratories may vary in detail, but they all consist of the following basic components: 1) A scanning electron microscope column which produces the focused incident electron beam; 2) An ultra-high vacuum chamber with tools for surface preparation and analysis; 3) One or more spin polarization analyzers; 4) Electron optics for collecting and transporting the emitted secondary electrons to the detectors; And, 5) some form of image processing to transform the polarization measurements into magnetization images. All of these components are described in detail elsewhere [11.10,32,33] so that the instrumentation will only be briefly reviewed here.
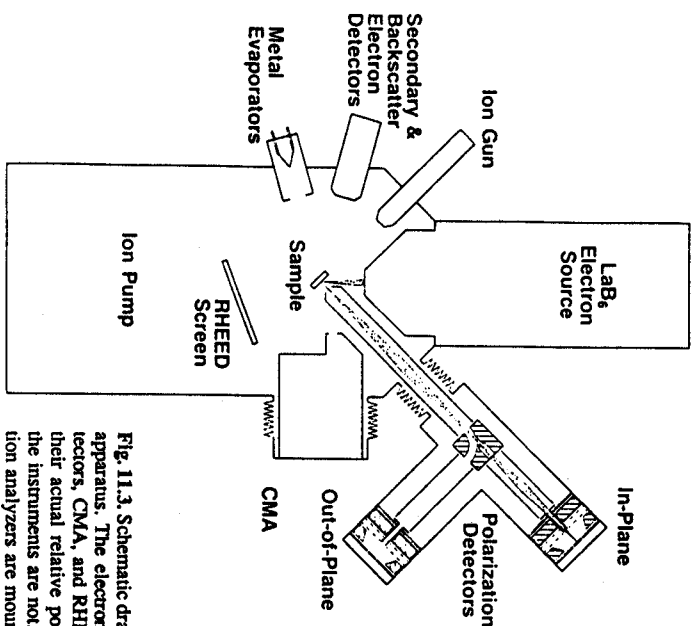
11.2.1 Electron Microscope and Specimen Chamber

An electron microscope with a high brightness electron source is desirable, because of the inefficiency of existing electron spin polarization analyzers. The minimum beam current required to obtain a SEMPA image in a reasonable amount of time is about 1nA. For a LaB6 cathode, such as the one used on the NIST SEMPA apparatus, 1 nA corresponds to a nominal beam diameter of about 40 nm. Smaller probes can be formed using either cold or thermally assisted field emission sources [11.34]. SEMPA instruments using field emission sources should have usable probes that are 10nm or less in diameter.

The incident beam energy used is a compromise between resolution and signal intensity. The secondary electron yield increases with decreasing beam energy [11.29], but the beam diameter also increases. In addition, a lower energy primary electron beam is more susceptible to deflections and distortions due to any electrostatic extraction fields or stray magnetic fields that may be present. Under typical operating conditions, a 10keV incident electron beam is used which produces a secondary yield that is about 20% of the incident current.

Two final considerations concerning the objective lens and the working distance between the objective lens and the sample and the stray magnetic field

Fig. 11.3. Schematic drawing of the NIST SEMPA apparatus. The electron source, polarization detectors, CMA, and RHEED screen are shown in their actual relative positions, while the rest of the instruments are not. The CMA and polarization analyzers are mounted on bellows

coming from the objective lens. A large working distance is desirable in order to provide access to the sample by the polarization analyzers as well as other surface analysis and preparation instruments. Unfortunately, the incident beam diameter increases with increasing working distance. A long working distance is also desirable in order to remove the sample from the stray magnetic field of the objective lens. This stray magnetic field can affect the secondary electrons by deflecting their trajectories and rotating their spins. In addition, a stray magnetic field can change the domain structure of the magnetic specimen. A working distance of about 10 mm and a stray field at the sample of one gauss or less are typical.

As a result of its surface sensitivity, the SEMPA technique requires that the microscope have a bakeable, ultra-high vacuum specimen chamber that is equipped with various devices for the in situ preparation and characterization of samples. The base pressure of the NIST SEMPA apparatus shown in Fig. 11.3 is 6×10^{-8} Pa. The chamber has an ion gun for cleaning samples, a heated stage for annealing the samples after ion bombardment, and metal evaporators for depositing magnetic or nonmagnetic thin films. The chemical composition of the surface is monitored by Auger electron spectroscopy using the cylindrical mirror energy analyzer. This apparatus can, therefore, generate compositional maps from the same areas that are imaged using SEMPA. The surface order is measured by tilting the sample and analyzing the reflection high energy electron diffraction (RHEED) patterns from the surface. In addition, the microscope can generate standard SEM images using either secondary electrons, backscattered electrons, or absorbed sample current. One feature that has not been implemented, but is highly desirable for certain magnetic studies, is some method for applying a magnetic field to the sample such that the secondary electron trajectories are not disturbed.

11.2.2 Transport Optics and Polarization Analyzers

The function of the spin polarization analyzer input optics is to collect as many of the emitted secondary electrons as possible, transport them to the analyzer with minimum loss of intensity or change in polarization, and deliver the electrons with the correct energy and momentum for analysis. The design of the input electron optics depends critically upon the type of polarization analyzer used and the specimen chamber geometry. In the NIST SEMPA apparatus [11.32] the front end of the input optics is biased at a positive 1500 volts in order to collect most of the low energy secondary electrons emitted from the sample. One problem with this biasing arrangement is that the sample and sample holder become part of the extraction electron optics, so that tilting the sample or changing the sample geometry can change the secondary electron trajectories. On the positive side, rapid acceleration of the secondaries minimizes any adverse effects from magnetic stray fields from the lens or sample. The transport optics is designed to transmit all of the accelerated secondary electrons within a 8 eV wide energy

window to the polarimeter. In practice, about 90% of these electrons are actually transmitted.

The input optics also contain deflection plates to descan the secondary electrons and a 90 degree electrostatic deflector to switch the electrons from one polarimeter to another. The purpose of the descan deflectors is to keep the motion of the incident beam at the sample from being transmitted to the polarimeter where the beam motion due to the scan can introduce false polarization signals especially at low magnifications (large scans). Descanning is accomplished by sensing the scan voltage of the SEM and driving the electrostatic deflection plates of the input optics with a voltage that is 180 degrees out of phase. A 90 degree deflector and two polarimeters are used so that all components of an arbitrary magnetization vector can be measured. Each polarimeter measures the two transverse polarization components of the electron beam. For the specimen-polarimeter geometry shown in Fig. 11.3, the undeflected, straight through analyzer measures the two in-plane components of the sample magnetization, while an orthogonal detector, accessed by activating the 90 degree deflector, measures the out-of-plane magnetization and a redundant in-plane component. The redundant component is used to ensure that both detectors have identical polarization sensitivities. Alternate methods for measuring all of the magnetization components using just one analyzer involve rotating the specimen [11.33, 35] or rotating the polarization with a Wien filter [11.36].

Various electron spin polarization analyzers are currently available. The choices include traditional 100 keV Mott detectors [11.37], 30 keV retarding Mott analyzers [11.38], low energy electron diffraction (LEED) analyzers [11.4], low energy diffuse scattering (LEDS) analyzers [11.39, 40], and low energy absorbed current detectors [11.41, 42]. The features and relative merits of the various analyzers have been discussed in detail elsewhere [11.32, 43]. Fully operational SEMPA instruments have been constructed using a Mott analyzer [11.44], a LEED analyzer [11.33], and a LEDS analyzer [11.11].

The basis for the spin sensitivity of most of the polarization analyzers is the spin-orbit interaction [11.1]. When an electron scatters from the central potential of some high atomic number atom, there is an additional interaction between the electron's spin and its orbital angular momentum about the central potential. The spin-orbit interaction has the effect of making the scattering cross sections different for electrons with spins parallel or anti-parallel to the scattering plane normal. The scattering plane is the plane in which both the incident and scattered electron trajectories lie. The simplest polarization analyzer, therefore, consists of a high-Z target and two electron detectors, one measuring the number of electrons scattered to the right, the other to the left. An incident beam of electrons with a polarization component P perpendicular to the scattering plane would result in a scattering asymmetry A

$$A = \frac{N_L - N_R}{N_L + N_R} = PS ,$$

(11.4)

where $N_L(N_R)$ are the number of electrons scattered to the left (right) detector

and S, the Sherman function, is a parameter which describes the analyzer's sensitivity to polarization.

The performance of a polarization analyzer is characterized by the Sherman function and the fraction of incident electrons scattered into the detectors, I/I_0. The figure of merit F for a spin polarization analyzer in a measurement limited by counting statistics is given by

$$F = (I/I_0)S^2 .$$

(11.5)

For optimized analyzers, F is approximate 1×10^{-4}. In practice, this means that it will take 10^4 times as long to acquire a polarization measurement as an intensity measurement with the same statistics. For comparison, a typical Auger measurement takes about 10^6 times as long as an intensity measurement [11.45].

In selecting a particular spin polarization analyzer, features other than the figure of merit must also be considered. Among these are proper electron optical coupling with the phase space of the electrons to be analyzed, immunity from false apparatus asymmetries, minimum disturbance to the functioning of the SEM, and ease of use. No single detector fully satisfies all of these requirements, so that some compromises have to be made. For example, high energy Mott detectors have the largest electron acceptance phase space, but the low energy polarimeters are much more compact and, therefore, easier to attach to an SEM. Further polarimeter comparisons can be found in the review papers [11.32, 43].

A schematic drawing of the low energy diffuse scattering (LEDS) analyzer used on the NIST SEMPA apparatus is shown in Fig. 11.4. It is based on the scattering of 150 eV electrons from an evaporated polycrystalline Au target. The Au films are evaporated in situ and are stable for at least a week in ultrahigh vacuum. The incident electrons are scattered diffusely from the polycrystalline surface. A negatively biased electrode E_1 focuses the scattered electrons into a pair of retarding grids, G_1 and G_2, which filter out the low energy secondary electrons generated at the Au target. After passing the grids, the electrons proceed to a microchannel plate electron multiplier. The amplified signal is then detected by an anode which is divided into four equal quadrants as shown in the inset of Fig. 11.4. The two orthogonal transverse polarization components of the incident beam are measured simultaneously and are given by

$$P_z = \frac{1}{S}\frac{N_A - N_C}{N_A + N_C} ,$$

(11.6)

$$P_y = \frac{1}{S}\frac{N_B - N_D}{N_B + N_D} ,$$

(11.7)

where N_i is the number of electrons counted by quandrant "i".

A common problem of electron spin polarimeters is the elimination of any false polarization signals due to instrumental asymmetries. Instrumental asymmetries can be the result of intrinsic nonuniformities in the detector such as differences in gain and zero signal levels between different detector channels and mechanical deviations from a symmetric scattering geometry. These instru-
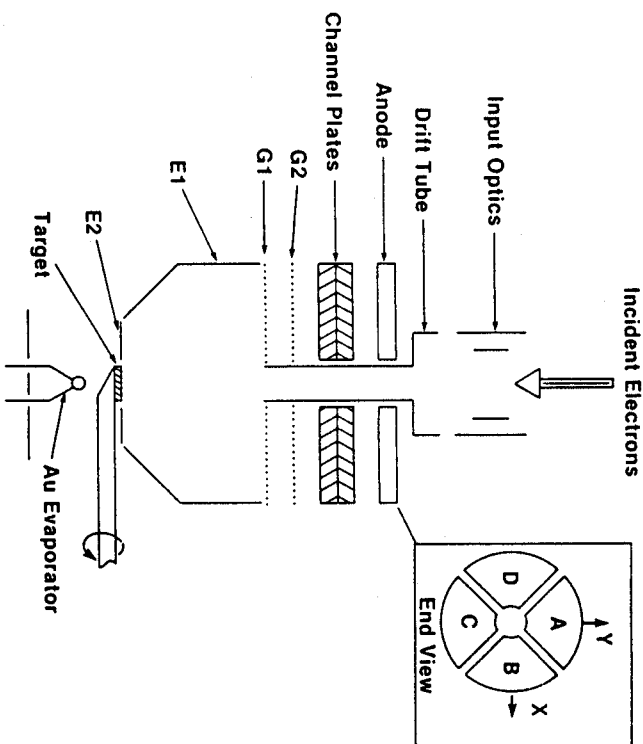
Fig. 11.4. Schematic drawing of a low energy diffuse scattering spin polarization analyzer. The inset shows how the anode is divided into quadrants so that polarization components along both the x and y directions may be measured simultaneously

mental asymmetries are relatively easy to eliminate by using the unpolarized electrons from a non-magnetic sample for calibration and standard electronic and mechanical design practices. Another source of false asymmetry is the sensitivity of the polarimeter to incident electron trajectories. If the position or angle of the incident electron beam at the high-Z scattering target changes, then opposing electron counters will record different relative intensities and, therefore, measure a false polarization. Deviations of the electron beam trajectories at the detector can be caused by scanning of the incident electron beam at the sample, variations in the electrostatic extraction field due to sample geometry, topography, or work function, and stray magnetic fields from the objective lens and the specimen. These instrumental asymmetries are much more difficult to eliminate because they can be different for each polarization measurement.

In the NIST SEMPA apparatus, trajectory related instrumental asymmetries are reduced using several techniques. First, the scan of the primary electron beam is removed by descanning the secondary electron beam in the analyzer input optics. Second, the detector uses an electron optical compensation scheme which balances spatial and angular components of the instrumental asymmetry [11.40]. In the compensation scheme, electrostatic lenses are set such that a change in position of the beam at the target is balanced by a change in the incident angle and the angular change in the asymmetry is equal and opposite to

the spatial one. These first two methods can eliminate instrumental asymmetries from most SEMPA measurements. Any remaining false asymmetries, such as those associated with very rough specimens, can be removed by using a low-Z graphite reference target in the polarimeter so that the spin dependence of the polarimeter can be turned off without changing the instrumental asymmetries. In these cases, a reference measurement is made using the graphite target for every polarization measurement using the Au target, and the difference between them is the true polarization. An example of this process will be described in a later section.

11.2.3 Image Processing

The final product of SEMPA is a picture of the direction and magnitude of the magnetization in the area scanned by the SEM. Unlike conventional microscopies, which display a scalar quantity such as the secondary electron intensity in the standard SEM image, SEMPA produces an image of a vector quantity, the magnetization. Therefore, the SEMPA image processing system must not only be able to perform standard image processing tasks such as data storage, display, filtering, and background subtraction, but, in addition, the system must be able to combine the individual polarization measurements into maps of the magnetization vector field [11.46]. For example, the polarimeters can measure two in-plane magnetization components, M_x and M_y, and an out-of-plane component, M_z. In order to determine the direction and magnitude of the magnetization, the image processing system must be able to remove any residual instrumental asymmetry offsets, check for registration of the images by cross correlation techniques, and produce images of the magnitude

$$|M| = \sqrt{M_x^2 + M_y^2 + M_z^2} \tag{11.8}$$

and the direction of magnetization within the surface plane

$$\Theta_{ip} = \tan^{-1}\frac{M_y}{M_x} \tag{11.9}$$

or out of the surface

$$\Theta_{op} = \tan^{-1}\frac{M_z}{\sqrt{M_x^2 + M_y^2}}. \tag{11.10}$$

In addition, the image processing system should be able to generate quantitative information such as, line scans, histograms, and scatter plots [11.47] from the SEMPA data.

11.3.1 Iron Crystals

Because of their large intrinsic secondary polarization and well known bulk magnetic properties, Fe crystals are good specimens for demonstrating various SEMPA features [11.3,8,9,10,11,33,46,48–53]. Figure 11.5 shows SEMPA measurements of the domain structure of the {100} surface of an Fe-3%Si crystal. The surface was prepared by ion sputtering with 1 keV Ar ions followed by annealing to 700°C. The small amount of Si present in the sample makes cleaning easier by suppressing the bcc to fcc phase transition of pure Fe. Figure 11.5a shows the horizontal in-plane magnetization component, M_x. The brightness of the image is linearly proportional to the magnetization component. In the grey scale of the M_x image, positive magnetization points to the right and is mapped to white while negative magnetization points to the left and is mapped to black. Figure 11.5b shows the corresponding vertical magnetization component, M_y, with white corresponding to magnetization pointing up and black pointing down. The secondary intensity image, which is simply equal to the denominator,
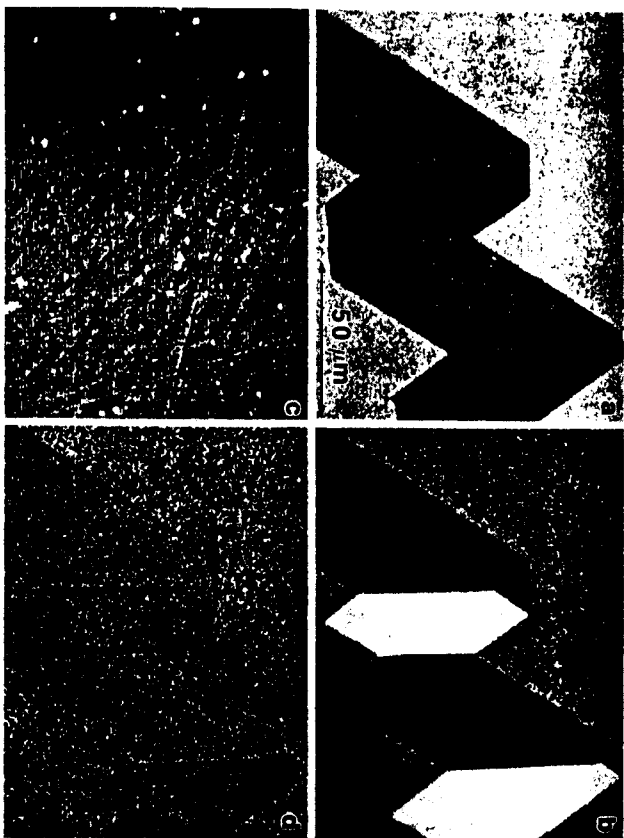

Fig. 11.5a–d. An example of a SEMPA measurement showing the domain structure of the {100} surface of an Fe-3%Si crystal. The (a) horizontal, M_x, and (b) vertical, M_y, in-plane magnetization components are shown along with (c) the simultaneously measured intensity topograph. The magnitude of the magnetization computed from the components is shown in (d)

$N_A + N_C$, of the polarization in (6), is shown in Fig. 11.5c. M_x, M_y and the intensity are all measured simultaneously by one detector.

The 256 × 192 pixel images in Fig. 11.5 are 140 μm across. The measurements were made using an incident beam current of 15.5 nA and a dwell time of 4.0 ms/pixel, so that the images took about four minutes to acquire. No out-of-plane, M_z, component was observed. The domain structure is primarily determined by the fact that Fe, a material with cubic anisotropy, has two orthogonal easy magnetization axes that lie in the {100} surface and one which is perpendicular to the surface. Any magnetization component pointing out of the plane, however, is associated with a large magnetostatic energy. The magnetization therefore remains in-plane and lies along one of the two orthogonal easy axis.

One feature of the Fe SEMPA data that is common to all SEMPA measurements is that the magnetic and topographic images can be separated. The secondary electron intensity and polarization are measured simultaneously, but they are completely independent measurements. SEMPA is therefore a useful technique for studying the relationships between topographic and magnetic structure. For example, SEMPA has been used to observe the pinning of domain walls by point defects within a ferromagnet [11.12].

The individual magnetization components can be used to calculate the magnitude and direction of the in-plane magnetization. First, the instrumental asymmetry offset is removed by subtracting a plane from the image so that domains of opposite magnetization corresponded to equal but opposite values of polarization. This is based on assuming a constant magnetization magnitude for the entire image. The magnitude of the magnetization is then calculated, as shown in Fig. 11.5d. It is essentially constant which verifies that the instrumental asymmetry was correctly removed. There appears to be some magnetization missing at the domain walls, but this is purely an instrumental artifact due to the finite size of the beam. When the incident electron beam diameter, in this case about 200 nm, is larger than the domain wall, the polarization measurement averages over domains with magnetization components of opposite direction, leading to a reduced value for the magnitude of the magnetization [11.32]. The direction of the magnetization is shown by the in-plane angle image in Fig. 11.9a. The direction of the magnetization components is displayed by calculating the angles from the value of the magnetization components and mapping these angles into color using the color wheel shown in the inset of Fig. 11.9. In this representation, the two easy magnetization axes are obvious.

In some cases, specifically, when large topographic features are present, spurious instrumental asymmetries can only be removed by using magnetization independent reference images obtained with the graphite target in the analyzer. This procedure is illustrated by SEMPA images from single crystal Fe whiskers shown in Fig. 11.6. The whiskers were cleaned by Ar ion bombardment and

Fig. 11.6a–h. SEMPA measurements of magnetic domains in an Fe whisker which demonstrate how spurious instrumental asymmetries can be removed using a graphite reference target in the detector. (a) and (b) SEMPA measurements of M_x and M_y are made using a Au target; (c) and (d) using a graphite target; (e) and (f) after subtracting the graphite data from the Au. (g) The magnetization magnitude and (h) intensity are also shown
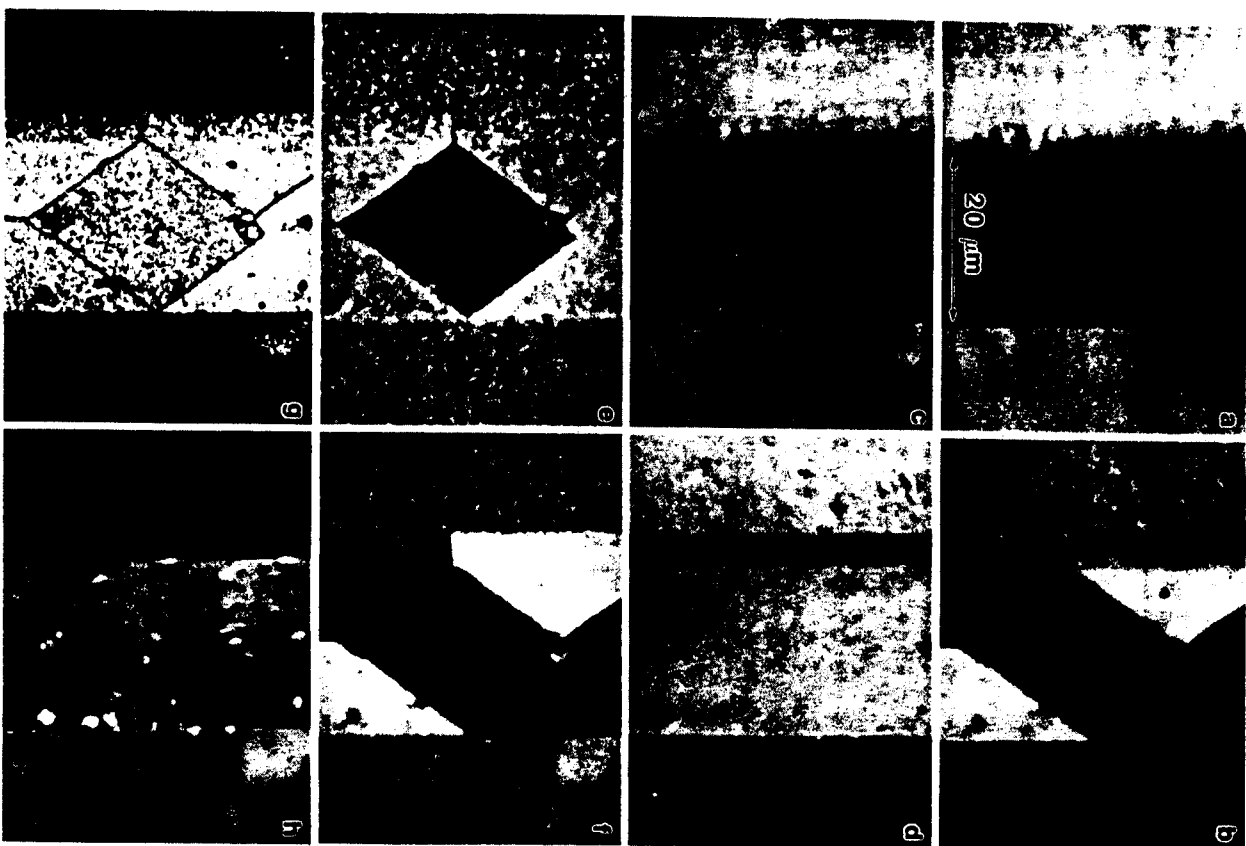
Fig. 11.6a–h. Caption see opposite page

700°C annealing. The whiskers are grown along the (100) direction with sides that are {100} surfaces. The whiskers are about 20 μm wide by several mm long. They are mounted on a nonmagnetic sample holder which is visible to the right and left of the whisker. Unprocessed SEMPA images of the in-plane magnetization components are shown in Figs. 6a and b. The intensity is shown in Fig. 6h. Although the domain structure of the whisker is clearly visible, the unprocessed magnetization images contain several artifacts due to sample topography. Examples of these artifacts include the non-zero polarization signals from the sample holder, the polarization level from the top of the sample differs from the side, and surface roughness "feed through" into the magnetization signal. Figures 6c and d show the same areas of the sample measured using a graphite target in the polarimeter. Figures 6e and f show the magnetization components after subtracting the graphite data. Inspection of these images shows that the instrumental artifacts have been greatly reduced. This can also be observed in the magnitude of the magnetization shown in Fig. 6g; the magnetization is essentially constant over the top and side of the whisker and equal to zero on the sample holder. The remaining regions of low magnetization on the sample are due to nonmagnetic contamination.

A final example of a SEMPA measurement of an Fe whisker is shown in Fig. 11.7. Two important features of SEMPA are illustrated by this measurement, which shows both the diamond shaped domain on the top of the tilted sample and the associated zig-zag domain wall running down the side. First, because SEMPA uses an electron microscope to form the electron probe, the technique has excellent depth of focus making it useful in non-planar geometries. Secondly, this measurement emphasizes that SEMPA, like all of the other domain imaging techniques, only looks at the surface closure domain structure. The bulk domain structure of this whisker is the diamond domain observed from the top. This bulk structure is not at all obvious from the zig-zag closure domain structure observed along the side.
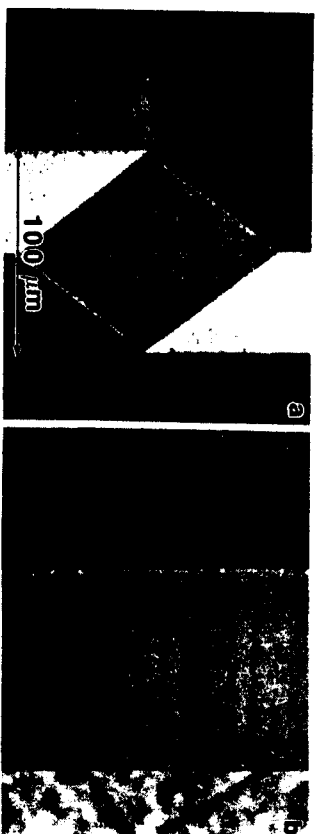

Fig. 11.7a,b. A SEMPA measurement showing (a) M_y and (b) the intensity from an Fe single crystal whisker demonstrating the technique's depth of focus. Domains are clearly visible on the top and side of this tilted sample which has a rectangular cross section

11.3.2 Cobalt Crystals

The domain structure of cobalt is primarily determined by its uniaxial crystalline anisotropy. The easy magnetization axis of a *hcp* cobalt crystal is along the c axis. SEMPA has been used to investigate domains on Co surfaces with the c axis lying in plane [11.10, 44, 48, 51] and normal to the surface plane [11.46, 54]. SEMPA measurements of the Co{0001} surface are especially interesting because the strong c axis crystalline anisotropy results in a magnetization component that is perpendicular to the surface. Figure 11.8 shows all three magnetization components and the intensity for the Co{0001} surface. A positive perpendicular magnetization component, M_z, corresponding to magnetization pointing out of the surface, is colored white in Fig. 11.8. Black corresponds to magnetization pointing into the surface. The images are 10 μm across and took about 25 minutes to acquire. The Co surface was cleaned by Ar ion bombardment followed by annealing to 400°C. As can be seen from the SEMPA images the domain microstructure is rather complex [11.54]. Even with an easy magnetization axis perpendicular to the surface, the large amount of magnetostatic energy associated with a perpendicular magnetization forces the magnetization to primarily lie in plane. The result is a surface magnetic microstructure, which consists of
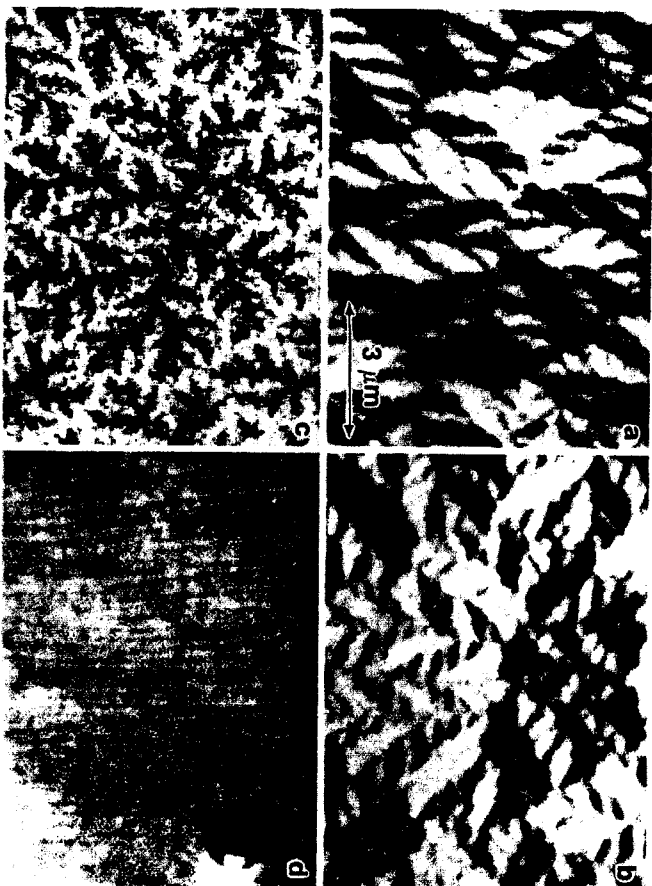

Fig. 11.8a–d. Domain structure of the {0001} surface of Co. The magnetization has in-plane components, (a) M_x and (b) M_y, and (c) an out-of-plane component, M_z. (d) Intensity topograph
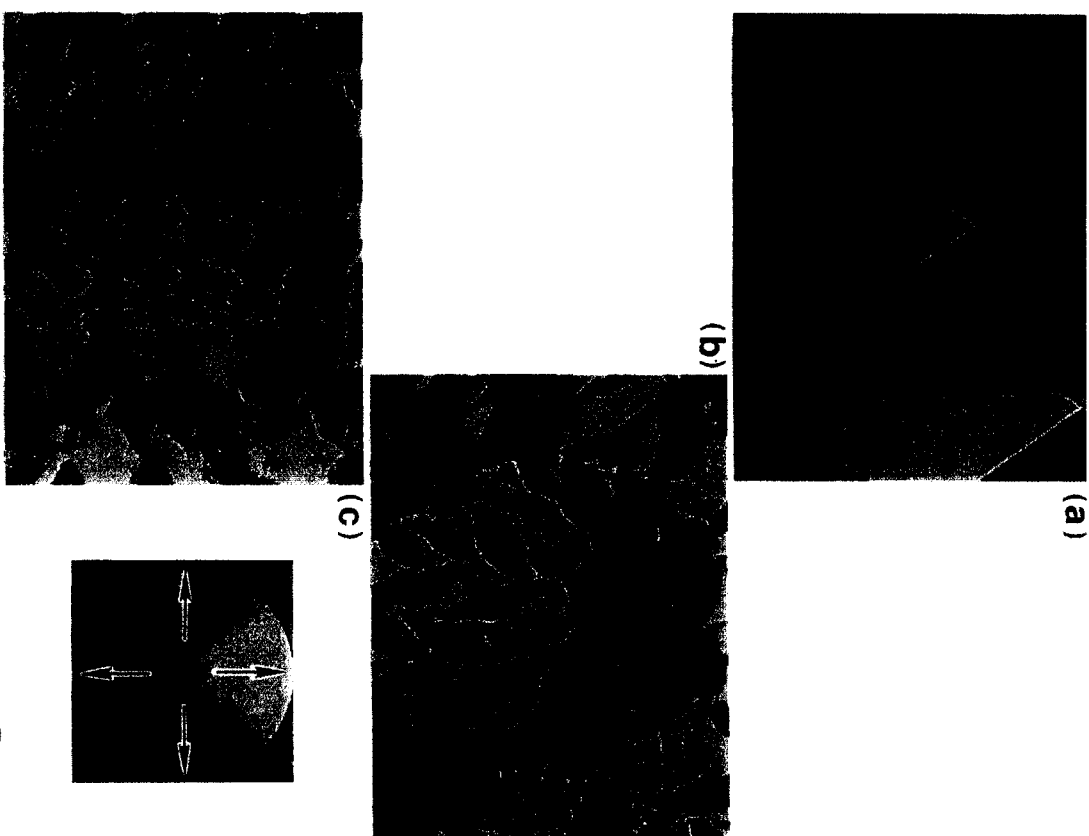
(a)

(b)

(c)

(d)

Fig. 11.9a–d. SEMPA images showing the direction of the in-plane magnetization in (a) Fe-3%Si {100}, (b) Co {0001}, (c) a stressed ferromagnetic glass, and (d) a NiFe thin film with a cross tie domain wall. Magnetization directions are represented by colors as shown in the color wheel in the inset

narrow, branched regions of perpendicular magnetization separated by regions of in-plane magnetization. The magnetization direction varies continuously as the magnetization comes to the surface, flows along the surface, and returns into the bulk. The relationship between the in-plane and out-of-plane domain structures is easier to visualize by comparing the M_z image in Fig. 11.8c with the map of the in-plane magnetization direction which is shown in Fig. 11.9b. The map of the in-plane magnetization angle also shows that the in-plane magnetization has a domain substructure that appears to reflect the sixfold symmetry of the Co{0001} surface.

11.3.3 Ferromagnetic Metallic Glasses

Because of the long range nature of magnetic interactions, measurements of the surface domain microstructure of a magnetic sample can, in some cases, yield useful information about the internal bulk properties of the material. One example of this use of domain imaging is in the determination of internal stresses in ferromagnetic metallic glasses [11.55, 56]. Because crystalline order is missing in the ferromagnetic glasses, they do not have an easy magnetization axis associated with magnetocrystalline anisotropy. This lack of strong anisotropy results in their useful magnetic properties such as, low coercivity, low losses, and high permeability. Magnetic domains in these materials are generally large with weak shape anisotropies determining the orientation of the domains. When the glasses are strained, however, magnetostrictive interactions cause anisotropies which lead to the development of a fine domain pattern. Investigations of the surface domain structure, therefore, yield information about the strains within the ferromagnetic glass and about how different kinds of stresses affect their magnetic properties.

SEMPA measurements of the domain structure in a stressed $Fe_{81}B_{13.5}Si_{3.5}C_2$ metallic glass (Allied 2605SC) are shown in Figs. 11.9 and 11.10. The glass was plastically deformed by bending which produced the black and white shear bands
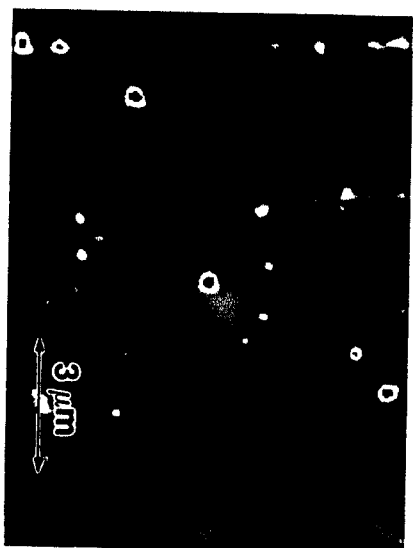

Fig. 11.10. Intensity topograph of a stressed ferromagnetic glass. The vertical lines are shear bands. The corresponding domain structure is shown in Fig. 11.9c

that are visible in the topograph in Fig. 11.10. The domain structure from the same region is shown in Fig. 11.9c. Detailed analysis of the domain structure reveals information about the microstructural properties of the shear bands [11.57].

11.3.4 Domain Walls

A particularly useful feature of the SEMPA technique, when compared with other methods of imaging domains, is that SEMPA can not only produce pictures of the domain structure but also provide quantitative information about the magnetization. SEMPA is, therefore, an appropriate measurement technique for testing various theoretical predictions of magnetic microstructure. One example of this work is the study of the width and the internal structure of domain walls at surfaces.

Within the bulk of a thick ferromagnet the boundary between antiparallel domains is a 180° Bloch wall, in which the magnetization rotates in the plane of the wall. If the Bloch wall were terminated by a surface, the magnetization would point out of the surface causing a large, energetically unfavourable stray field. In a thin film, this surface magnetostatic energy is sufficient to force the magnetization to rotate totally within the plane of the film, forming a Néel wall [11.58]. Because of the magnetostatic energy contribution associated with the surface, it has been predicted [11.59, 60] that, even in a thick ferromagnet, Bloch-like domain walls in the bulk would terminate as Néel walls at the surface. These Néel wall "caps" have been observed using magneto-optic Kerr microscopy [11.61] and SEMPA [11.10,11,33,62]. SEMPA images of domain walls in a Co-based ferromagnetic glass are shown in Fig. 11.11 [11.62]. Only in-plane magnetization components are observed, clearly showing Néel wall behavior at the surface. A Bloch wall would show contrast in the out-of-plane component, which is not observed. Instead, contrast in the horizontal in-plane component is observed. Note that there can be two opposite senses to the rotation of the magnetization within the walls, which results in either black or white contrast in the horizontal component image, Fig. 11.11d.

Because of its spatial resolution, SEMPA measurements provide a stringent test of model calculations of surface domain wall configurations. The calculations are described in detail elsewhere [11.62,63]. Basically, the calculations involve minimizing the total magnetic energy, which includes contributions from exchange, anisotropy and magnetostatic energy. Only well-known, bulk magnetic properties were used as input parameters for these calculations. The results for the calculation of the magnetization distribution in a cross section of an Fe crystal are shown schematically in Fig. 11.12. The cross section shows a bulk Bloch wall which turns over into a Néel wall at the surface. Domain wall profiles were measured for a 20 µm thick single crystal Fe whisker, a 1200 Å thick $Ni_{80}Fe_{20}$ Permalloy film, and a 2400 Å thick $Ni_{80}Fe_{20}$ Permalloy film. Calculated and measured wall profiles of the in-plane component of the magnetization perpendicular to the wall are shown in Fig. 11.13. The agreement between the measured and calculated wall profiles is impressive, especially, considering the large variation
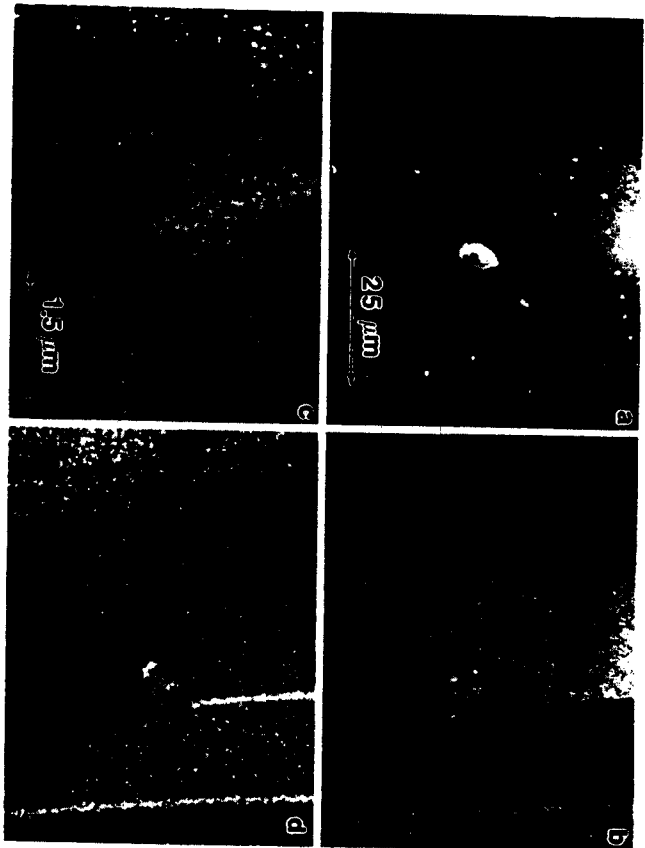
Fig.11.11a–c. SEMPA images of domain walls in a Co based ferromagnetic glass. Shown are (a) the intensity, (b) M_y, (d) M_z, and (c) a magnified image from the region where the wall changes chirality
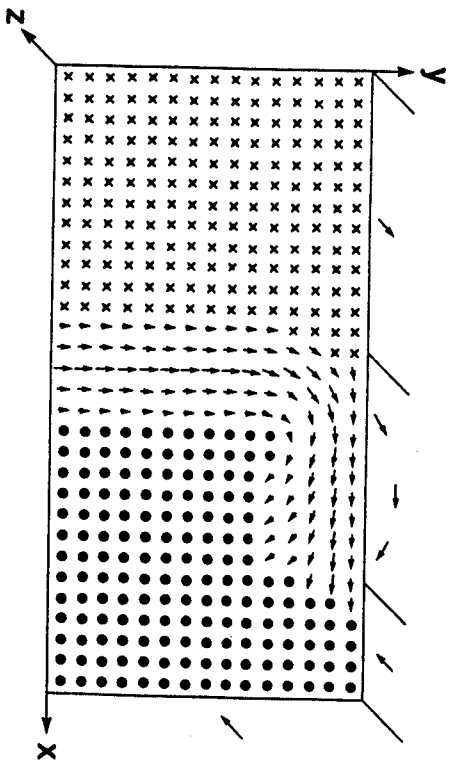
25 μm

1.5 μm

Fig.11.12. Schematic representation of a calculated magnetization distribution in the upper 0.2 μm of the cross section through an Fe sample. The domain wall is a Bloch wall in the solid, but rotates into a Néel wall at the surface

z

y

x

M_x/M_s

1.0   0.6   0.2   -0.2

Fe   (a)

-0.4   -0.2   0.0   0.2   0.4

M_x/M_s

1.0   0.6   0.2   -0.2

NiFe 1200 Å   (b)

-0.4   -0.2   0.0   0.2   0.4

M_x/M_s

1.0   0.6   0.2   -0.2

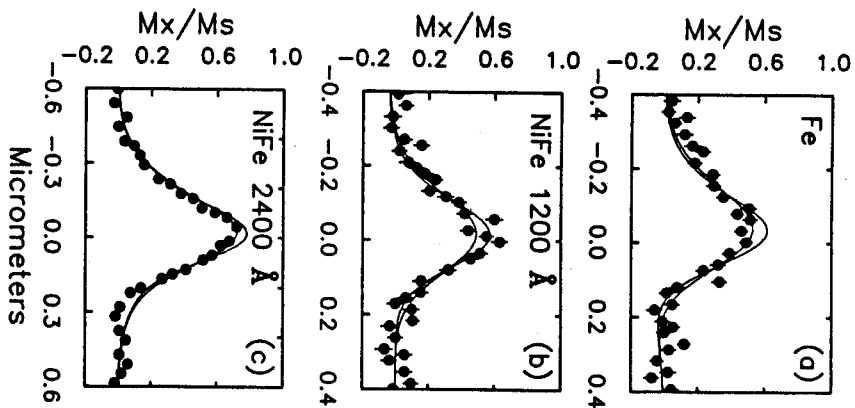NiFe 2400 Å   (c)

-0.6   -0.3   0.0   0.3   0.6

Micrometers

Fig.11.13a–c. Comparison of calculated and measured profiles of the magnetization component perpendicular to the wall for (a) an Fe {100} single crystal, (b) a 1200 Å thick $Ni_{80}Fe_{20}$ Permalloy film, and (c) a 2400 Å thick Permalloy film

in magnetic properties between these various materials. Similar calculations and measurements were also made for other $Ni_{80}Fe_{20}$ films as a function of film thickness, and again there was good agreement between calculated and measured wall widths [11.64]. Because of this excellent agreement, the magnetic models can be used with confidence to predict magnetization distributions in other systems. For example, the model can be used to interpret the results of TEM Lorentz measurements which average over the thickness of a sample, or understand the interactions between the tip and sample in magnetic force microscopy measurements [11.63].

In addition to measurements of domain wall widths, SEMPA can be used to study other magnetic microstructural phenomena associated with domain walls. An example of such a structure is the magnetic singularity shown in Fig. 11.1c. The singularity is associated with a change in the chirality of the domain wall. The in-plane magnetization swirls about this singularity in a clockwise direction. At the center of the singularity the topology does not permit a non-zero in-plane magnetization component, so that the magnetization must either go to zero or

be forced into or out of the plane. Either case would be extremely interesting to observe, but the current spatial resolution of SEMPA only permits placing an upper limit of 65 nm on the radius of the singularity on a Co based ferromagnetic glass [11.65]. This is still about three times as large as predicted by model calculations [11.66]. Another question is whether the singularity occurs only at the surface. Then the surface Néel wall changes chirality but the underlying Bloch wall does not. If it penetrates into the bulk, then both the surface Néel and the bulk Bloch wall switch, forming a Bloch line [11.67]. Both cases can occur and SEMPA can be used to differentiate between them by measuring the lateral displacement of the surface Néel wall at the singularity. When only the surface wall changes chirality, there is a shift in the position of the domain wall at the singularity. This is the case in Fig. 11.11c. The shift is simply a result of the surface Néel wall being offset slightly from the bulk Bloch wall as shown in Fig. 11.12. When both the surface and bulk domain walls change chirality, no lateral shift in the surface domain wall position is observed.
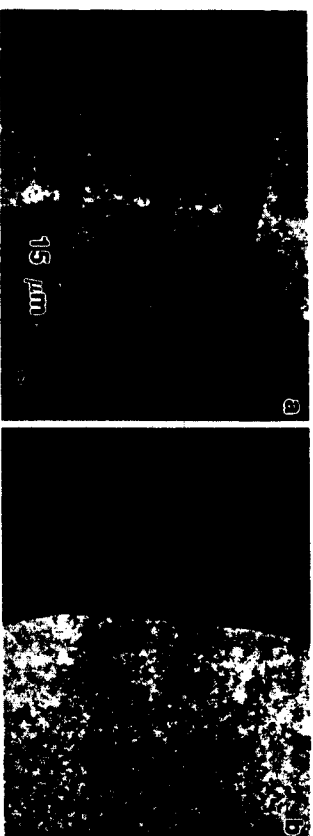

Fig. 11.14. SEMPA images of "Cross Tie" domain walls in a NiFe thin film showing (a) M_x and (b) M_y magnetization components

As a final example of how complicated domain wall structures can become, Figs. 11.14 and 11.9d show SEMPA measurements of "cross-tie" domain walls in a 40 nm thick $Ni_{80}Fe_{20}$ film. A single cross-tie, of which there are three in the figure, consists of two changes in domain wall chirality and hence two singular points [11.58]. The pair of singularities differ in that the magnetization forms a vortex about one but diverges from the other. The existence of cross-ties is a function of the film thickness and the applied magnetic field. Cross-ties occur in Permalloy films that are between 10 nm and 100 nm thick. Besides their scientific interest, most of the domain wall structures, such as cross-ties and Bloch lines, have potential uses in various magnetic memory devices where their small size makes them ideal for high density storage.

11.3.5 Magnetic Storage Media

One of the major driving forces behind magnetics technology today is the search for ways to store the maximum amount of information in the smallest space. One result of this push toward high density magnetic storage is that the physical size of the basic unit of information, a logical bit, has become smaller than can be imaged by conventional domain observation techniques. Bit dimensions are currently on the order of a μm, an will tend toward a tenth of a μm in the near future. In order to be a useful analytical tool for examining magnetic recording media, a domain observation technique must be able to image the recorded bits with sufficient resolution to not only see the bit but also resolve the transition region between bits. The quality of the recording media, in terms of the signal-to-noise during reading, is a sensitive function of the sharpness of the transition between bits. For example, in a conventional hard disc memory unit, bits written with poorly resolved transitions will yield lower signals when read by an inductive or magneto-resistive read/write head. Because of the high spatial resolution and the ability to look at as-deposited opaque samples, SEMPA is a useful technique for examining the magnetic microstructure of written information in conductive recording media. This information can be correlated with measurements of macroscopic magnetic properties in order to understand the recording characteristics of the media on a microscopic level.

SEMPA measurements of bits written on commercial memories have so far been limited to hard disc recording media composed primarily of Co-Ni alloy thin films with in-plane magnetization [11.10, 11.32, 11.68]. An example of how SEMPA can be used to understand the difference in recording characteristics between various media is illustrated in Fig. 15. The intensity topograph and the component of the magnetization approximately along the recorded track are shown for two different media compositions. Figure 11.15a,b correspond to a $Co_{26}Cr_{12}Ta_2$ film in which the bits were read with good signal-to-noise ratios. Figure 11.16c,d correspond to $Co_{75}Ni_{25}$ films that were noisier to read. The SEMPA images show that the reason for the poorer performance of the $Co_{75}Ni_{25}$ film is that the bits are not separated into distinct domains, but instead are randomly bridged together. In the good media the bits are more clearly separated.

Information can also be stored in magnetic media by using a focused laser beam to write and read the bits [11.69]. Briefly, writing a bit involves heating the media in an applied field. Bits are read by sensing the rotation of polarized light reflected from the surface. The materials involved are not the simple transition metal ferromagnets as discussed so far, but are transition metal-rare earth ferrimagnets in which the transition metal and the rare earth are magnetized in opposite directions. At a particular temperature, referred to as the compensation point, the two magnetic subsystems have equal magnetizations and, therefore, the net magnetization of the material is zero. Since compensation points are usually near room temperature, imaging domains with observation techniques that are sensitive to the net magnetization or field can be difficult. SEMPA has the useful feature that it is primarily sensitive to the magnetization of the transition metal. A
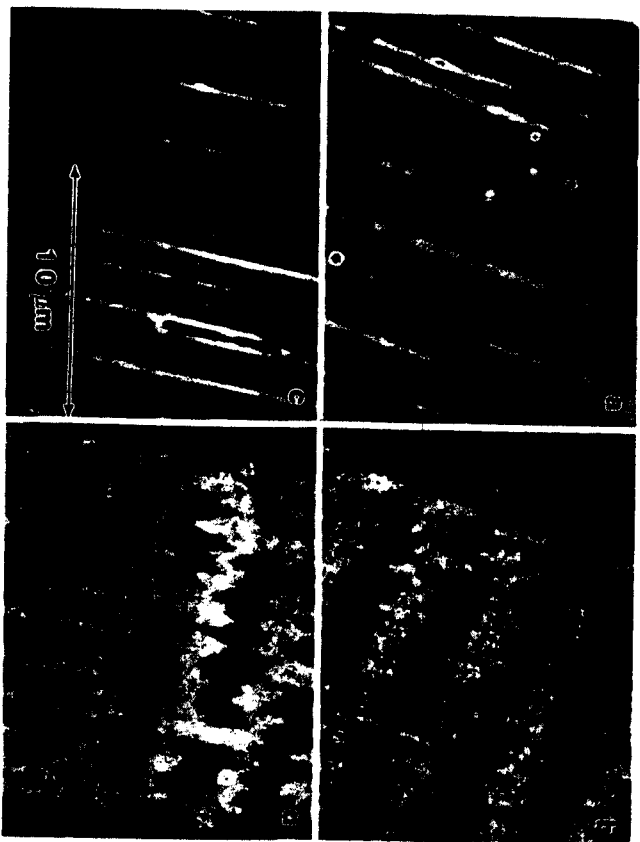
Fig. 11.15a–d. SEMPA images of bits written on thin film hard disc media of two different compositions. The topography and M_y are shown for a sample with good recording properties in (a) and (b), and for a sample with noisier, less well resolved bits in (c) and (d)

possible explanation is that only the weakly bound polarized valence electrons of the transition metal contribute to the secondary electron cascade while the more localized magnetic $4f$ electrons of the rare earth do not. This feature allows SEMPA to be used for imaging magnetic structures in rare earth–transition metal ferrimagnets even at the compensation point.

Figure 11.16 shows SEMPA measurements of magnetic domains written using a focused laser beam in a magneto-optic storage media, $Tb_{23.6}Fe_{67.6}Co_{8.8}$ (214 K compensation temperature) [11.70]. In this case, as with most magneto-optic media, the magnetization of the bulk material is perpendicular to the surface. The SEMPA measurements, however, show that there is also a sizable component of the magnetization lying in the plane of the surface. In fact, the magnetization makes an angle of about 45° with respect to the surface. The angle of the magnetization at the surface was found to depend upon the amount of Fe in the surface. As the amount of Fe is increased, the magnetization becomes more in plane.
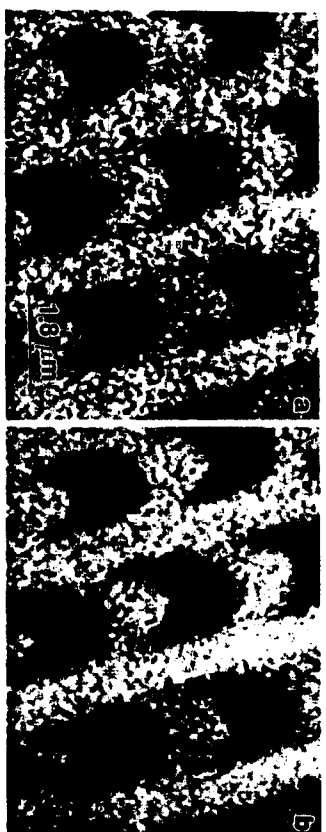

Fig. 11.16a,c. SEMPA images of bits written by a laser in a $Tb_{23.6}Fe_{67.6}Co_{8.8}$ magneto-optic recording media. The (a) M_x and (b) M_z magnetization components are shown

11.4 Summary and Future Directions

There are several features of SEMPA that make it an extremely powerful technique for the investigation of surface magnetic microstructure. First, the most important feature is that, because the polarization of secondary electrons emitted from a transition metal ferromagnet is directly proportional to the magnetization, SEMPA can directly measure the direction of the magnetization in a ferromagnet. SEMPA can, therefore, not only provide images showing the domain structure, but also quantitative information about the magnetization. Second, because SEMPA is based on a measurement of the electron spin polarization, a quantity that is independent of intensity, the magnetic structure can be separated from the topography. This separation permits investigations of the relationships between magnetic, topographic and, in some cases, chemical structures. Third, the technique is surface sensitive with a probing depth on the order of a nanometer. Surface sensitivity is an asset for studying thin films and surfaces, but the ultra-high vacuum requirements and extensive surface preparation are a drawback when only bulk magnetic structures are of interest. Finally, because SEMPA uses a scanning electron microscope as the incident probe, magnetic structures in opaque ferromagnetic samples can be imaged over a long depth of field with high spatial resolution (about 40 nm at present). The use of an electron probe does require that samples be electrically conducting in order to reduce charging and that stray magnetic fields near the sample must be held to a minimum (less than a few gauss) so that the secondary electron trajectories and polarizations are not disturbed.

Future improvements in SEMPA instrumentation will primarily be directed towards improving the spatial resolution and developing more efficient electron spin polarization analyzers. In the near future, the use of field emission electron sources along with optimized electron optics should push the spatial resolution of the technique to about 10 nm. Further major improvements in resolution may be difficult because of multiple scattering within the specimen which increase the

sampling volume. On the other hand, there is room for four orders of magnitude of improvement in the efficiency of the electron spin polarimeters. More efficient polarimeters would effectively improve the spatial resolution of SEMPA since less current would be needed and image acquisition times could be significantly shortened. There is sufficient contrast and intensity in the secondary electron signal so that television rate domain imaging would be possible if polarimeter efficiencies could be significantly improved. Unfortunately, only minor improvements in efficiency appear to be possible with the analyzers that are currently available.

Another potential area for improvement of the SEMPA technique involves the absolute quantification of the measurement; in effect, turning SEMPA into a surface magnetometer. Currently SEMPA measurements are proportional to the total magnetization. Absolute magnetization measurements will require some improvements in detector calibration, but primarily quantification will require more information about the secondary electron emission features such as sampling depth, effects of magnetic and non-magnetic adsorbates, and the energy and angle dependence of secondary electron polarization for various materials. Perhaps a short term solution will involve the use of calibration standards, such as those used in x-ray and Auger compositional analysis, in order to make more meaningful relative magnetization measurements.

Future work using SEMPA will be influenced by the fact that SEMPA has become a tested, routine method for the imaging of magnetic microstructures. One can, therefore, expect to see less work involving the development of the SEMPA technique and more emphasis on applying SEMPA to the myriad of technological and fundamental magnetics problems. One potentially fertile area of research that SEMPA is especially well suited for and that has barely been touched upon is the study of magnetic structures in films that are only a few monolayers thick. Because the films must be grown under ultra high vacuum conditions, SEMPA can be used to study the layer-by-layer development of the magnetic microstructure during film growth. Preliminary work in which domains in three monolayer thick Fe films were easily observed using SEMPA clearly show that SEMPA has the necessary surface sensitivity to observe magnetic structures in thin films [11.71]. SEMPA could be used to answer questions about whether domains exist in monolayer films, how layered thin film structures are magnetically coupled, and how the interlayer coupling is influenced by roughness and defects.

References

11.1 J. Kessler: *Polarized Electrons*, 2nd Ed. (Springer, Berlin, Heidelberg 1985)
11.2 R. Feder: *Polarized Electrons in Surface Physics* (World Scientific, Singapore 1985)
11.3 R.J. Celotta, D.T. Pierce: Science 234, 333 (1986)

11.4 J. Kirschner: *Polarized Electrons at Surfaces* (Springer, Berlin, Heidelberg 1985)
11.5 T.H. DiStefano: IBM Tech. Discl. Bull. 20, 4212 (1978)
11.6 J. Unguris, D.T. Pierce, A. Galejs, R.J. Celotta: Phys. Rev. Lett. 49, 72 (1982)
11.7 J. Kirschner: Scanning Electron Microsc. 1984, III: 1179 (1984)
11.8 K. Koike, K. Hayakawa: Jpn. J. Appl. Phys. 23, L187 (1984)
11.9 J. Unguris, G.G. Hembree, R.J. Celotta, D.T. Pierce: J. Microscopy 139, RP1 (1985)
11.10 K. Koike, H. Matsuyama, W.T. Pierce: Scanning Micro. Intern. Supp. 1 241 (1987)
11.11 G.G. Hembree, J. Unguris, R.J. Celotta, D.T. Pierce: Scanning Micro. Intern. Supp. 1, 229 (1987)
11.12 D.T. Pierce, J. Unguris, R.J. Celotta: MRS Bulletin 13(6), p. 19 (1988)
11.13 H.S. Williams, R.M. Bozorth, W. Shockley: Phys. Rev. 75, p. 155 (1949)
11.14 W. Rave, R. Schafer, A. Hubert: J. Magn. Magnet. Mat. 65(7) (1987)
11.15 B.E. Argyle, B. Petek, D.A. Herman, Jr.: J. Appl. Phys. 61, 4303 (1987)
11.16 D.E. Newbury, D.C. Joy, P. Echlin, C.E. Fiori, J.I. Goldstein: (Plenum New York, 1986) p. 147
11.17 J.P. Jakubovics: *Electron Microscopy in Materials Science Part IV*, ed. by E. Ruedl, U. Valdre (Commission of the European Communities, Brussels, 1973) p. 1305
11.18 J.N. Chapman, S. McVitie, J.R. McFadyen: Scanning Electron Microscopy Suppl. 1, 221 (1987)
11.19 A. Tonomura: J. Appl. Phys. 61, 4297 (1987)
11.20 Y. Martin, D. Rugar, H.K. Wickramasinghe: Appl. Phys. Lett. 52, 244 (1988)
11.21 J. Kirschner: In *Surface and Interface Characterization by Electron Optical Methods*, ed. by A. Howie, U. Valdre, (Plenum, New York, 1987) p. 267
11.22 E. Kisker, W. Gudat, K. Schröder: Solid State Commun. 44, 591 (1982)
11.23 H. Hopster, R. Raue, E. Kisker, G. Guntherodt, M. Campagna: Phys. Rev. Lett. 50, 70 (1983)
11.24 D. Penn, S.P. Apell, S.M. Girvin: Phys. Rev. Lett. 55(5), 518 (1985)
11.25 D.R. Penn, S.P. Apell, S.M. Girvin: Phys. Rev. B 32(12), 7753 (1985)
11.26 J. Kirschner: D. Rebenstorff, H. Ibach: Phys. Rev. Lett. 53, 694 (1984)
11.27 J. Glazer, E. Tosatti: Solid State Commun. 52, 905 (1984)
11.28 H. Hopster, R. Raue, R. Clauberg: Phys. Rev. Lett. 53, 695 (1984)
11.29 H. Seiler: J. Appl. Phys. 54, R1 (1983)
11.30 M.P. Seah, W.A. Dench: Surf. Interface Anal. 1, 2 (1979)
11.31 D.L. Abraham, H. Hopster: Phys. Rev. Lett. 58, 1352 (1987)
11.32 M.R. Scheinfein, J. Unguris, M.H. Kelley, D.T. Pierce, R.J. Celotta: Rev. Sci. Inst. (to be published)
11.33 H.P. Oepen, J. Kirschner: Phys. Rev. Lett. 62(7), 819 (1989)
11.34 J. Orloff: Ultramicr. 28, 88 (1989)
11.35 K. Koike, H. Matsuyama, H. Todokoro, K. Hayakawa: Scanning Micr. 1(1), 31 (1987)
11.36 M.R. Scheinfein: Optik 82(3), 99 (1989)
11.37 E. Kisker, R. Clauberg, W. Gudat: Rev. Sci. Instr. 53, 1137 (1982)
11.38 L.G. Gray, M.W. Hart, F.B. Dunning, G.K. Walters: Rev. Sci. Instr. 55(1), 88 (1984)
11.39 J. Unguris, D.T. Pierce, R.J. Celotta: Rev. Sci. Instr. 57(7), 1314 (1986)
11.40 M.R. Scheinfein, D.T. Pierce, J. Unguris, J.J. McClelland, R.J. Celotta: Rev. Sci. Instr. 60(1), 1 (1989)
11.41 D.T. Pierce, S.M. Girvin, J. Unguris, R.J. Celotta: Rev. Sci. Instr. 52(10), 1437 (1981)
11.42 K. Koike, H. Matsuyama, K. Hayakawa: Jap. J. Appl. Phys. 27(7), L1352 (1988)
11.43 D.T. Pierce, R.J. Celotta, M.H. Kelley, J. Unguris: Nuc. Instr. Meth. A266, 550 (1988)
11.44 K. Koike, K. Hayakawa: J. Appl. Phys. 57(1), 4244 (1985)
11.45 J.A. Venables, A.P. Janssen: Proc. of the 9th Int. Conf. on Electron Microscopy. Toronto (1978)
11.46 M.H.Kelley, J. Unguris, M.R. Scheinfein, D.T. Pierce, R.J. Celotta: Proc. of the Microbeam Analysis Society – 1989, ed. by P.E. Russell, (San Francisco Press, San Francisco 1989) p. 391
11.47 T. VanZandt, R. Browning, C.R. Helms, H. Poppa, M. Landolt: to be published in Rev. Sci. Inst.
11.48 K. Koike, H. Matsuyama, H. Todokoro, K. Hayakawa: Jap. J. Appl. Phys. 24(8), 1978 (1985)
11.49 K. Koike, H. Matsuyama, H. Todokoro, K. Hayakawa: Jap. J. Appl. Phys. 24(10), L833 (1985)
11.50 H.Matsuyama, K. Koike, H. Todokoro, K. Hayakawa, IEEE Translation Journal on Magnetics in Japan, TJMJ-1(9), 1071 (1985)

11.51 K. Hayakawa, K. Koike, H. Matsuyama: Hitachi Inst. News 14, 11 (1988)

11.52 G.G. Hembree, J. Unguris, R.J. Celotta, D.T. Pierce: Proc. of the 44th EMSA Meeting, ed. by G.W. Bailey, (San Francisco Press, San Francisco, 1986) p. 634

11.53 J. Unguris, G.G. Hembree, R.J. Celotta, D.T. Pierce: J. Vac. Sci. Technol. A5(4), 1976 (1987)

11.54 J. Unguris, M.R. Scheinfein, D.T. Pierce, R.J. Celotta: Appl. Phys. Lett. 55(24), 2553 (1989)

11.55 H. Kronmüller, W. Ferengel: Phys. Stat. Sol. (a) 64, 593 (1981)

11.56 J.D. Livingston: J. Appl. Phys. 57, 3555 (1985)

11.57 V. Lakshmanan, J.C.M. Li: Proc. of the Sixth Int. Conf. on Rapidly Quenched Metals, Mat. Sci. Eng. 98, 483 (1988)

11.58 B.D. Cullity: Introduction to Magnetic Materials, (Addison-Wesley, Reading, MA 1972) p.429

11.59 A. Hubert: Phys. Status Solidi B 32, 519 (1969)

11.60 A.E. LaBonte: J. Appl. Phys. 40, 2450 (1969)

11.61 F. Schmidt, W. Rave, A. Hubert: IEEE Trans. Mag. 21, 1596 (1985)

11.62 M.R. Scheinfein, J. Unguris, R.J. Celotta, D.T. Pierce: Phys. Rev. Lett. 63, 668 (1989)

11.63 M.R. Scheinfein, J. Unguris, D.T. Pierce, R.J. Celotta: Proc. of 34th Conf. on Magnetism and Magnetic Materials, Boston, MA.

11.64 M.R. Scheinfein, J. Unguris, P. Ryan, R.J. Celotta, D.T. Pierce: unpublished

11.65 M.R. Scheinfein, J. Unguris, R.J. Celotta, D.T. Pierce: International Workshop on the Magnetic Properties of Low Dimensional Systems, San Luis Potosi, Mexico, ed. by L.M. Falicov, J.L. Moran-Lopez, (Springer, Berlin, Heidelberg, November 1989)

11.66 A. Hubert: J. de Phys. Coll. C8, 49, 1865 (1988)

11.67 R. Schafer, W.K. Ho, J. Yamasaki, A. Hubert, F.B. Humphrey: Proc. of Intermag 1989, Washington, DC, to be published in IEEE Trans. Magn.

11.68 D.T. Pierce, M.R. Scheinfein, J. Unguris, R.J. Celotta: Materials Research Society Symposium Proceedings 151, 49 (1989)

11.69 M. Hartmann, B.A.J. Jacobs, J.J.M. Braat: Phillips Techn. Review 42, 37 (1985)

11.70 M. Aeschlimann, M.R. Scheinfein: private communication

11.71 J.L. Robins, R.J. Celotta, J. Unguris, D.T. Pierce, B.T. Jonker, G.A. Prinz: Appl. Phys. Lett. 52 (22), (1988)